

WavePID: Low-energy flavor identification using single-PMT time series in IceCube

R. Abbasi,¹⁵ M. Ackermann,⁶² J. Adams,¹⁶ J. A. Aguilar,⁹ M. Ahlers,²⁰ J.M. Alameddine,²¹ S. Ali,³⁴ N. M. Amin,⁴² K. Andeen,⁴⁰ C. Argüelles,¹² S. Athanasiadou,⁶² S. N. Axani,⁴² R. Babu,²² X. Bai,⁴⁸ A. Balagopal V.,⁴² S. W. Barwick,²⁸ V. Basu,⁵¹ R. Bay,⁵ J. J. Beatty,^{18,19} J. Becker Tjus,^{8,a} P. Behrens,⁰ J. Beise,⁶⁰ C. Bellenghi,²⁵ S. Benkel,⁶² S. BenZvi,⁵⁰ D. Berley,¹⁷ E. Bernardini,^{46,b} D. Z. Besson,³⁴ E. Blaufuss,¹⁷ L. Bloom,⁵⁷ S. Blot,⁶² F. Bontempo,²⁹ J. Y. Book Motzkin,¹² C. Boscolo Meneguolo,^{46,b} S. Böser,³⁹ O. Botner,⁶⁰ J. Böttcher,⁰ J. Braun,³⁸ B. Brinson,¹⁷ Z. Brisson-Tsavoussis,³¹ L. Brusa,²⁴ R. T. Burley,¹ D. Butterfield,³⁸ K. Carloni,¹² J. Carpio,^{32,33} N. Chau,⁹ Y. C. Chen,⁴² Z. Chen,⁵⁴ D. Chirkin,³⁸ S. Choi,⁵¹ A. Chubarov,²⁴ B. A. Clark,¹⁷ G. H. Collin,¹³ D. A. Coloma Borja,⁴⁶ A. Connolly,^{18,19} J. M. Conrad,¹³ D. F. Cowen,^{58,59} C. De Clercq,¹⁰ J. J. DeLaunay,⁵⁸ D. Delgado,¹² T. Delmeulle,⁹ S. Deng,⁰ P. Desiati,³⁸ K. D. de Vries,¹⁰ G. de Wasseige,³⁵ T. DeYoung,²² J. C. Díaz-Vélez,³⁸ S. DiKerby,²² T. Ding,^{32,33} M. Dittmer,⁴¹ A. Domi,²⁴ L. Draper,⁵¹ L. Dueser,⁰ D. Durnford,²³ K. Dutta,³⁹ M. A. DuVernois,³⁸ T. Ehrhardt,³⁹ L. Eidenschink,²⁵ A. Eimer,²⁴ C. Eldridge,²⁷ P. Eller,²⁵ E. Ellinger,⁶¹ D. Elsässer,²¹ R. Engel,^{29,30} H. Erpenbeck,³⁸ W. Esmail,⁴¹ S. Eulig,¹² J. Evans,¹⁷ P. A. Evenson,⁴² K. L. Fan,¹⁷ K. Fang,³⁸ K. Farrag,¹⁴ A. Fattorini,²¹ A. R. Fazely,⁴ A. Fedynitch,⁵⁶ N. Feigl,⁷ C. Finley,⁵³ D. Fox,⁵⁸ A. Franckowiak,⁸ S. Fukami,⁶² P. Fürst,⁰ J. Gallagher,³⁷ E. Ganster,⁰ A. Garcia,¹² M. Garcia,⁴² E. Genton,^{9,12} L. Gerhardt,⁶ A. Ghadimi,⁵⁷ C. Glaser,^{21,60} T. Glüsenkamp,⁵³ J. G. Gonzalez,⁴² S. Goswami,^{32,33} A. Granados,²² D. Grant,¹¹ S. J. Gray,¹⁷ S. Griffin,³⁸ S. Griswold,³⁸ K. M. Groth,²⁰ D. Guevel,³⁸ C. Günther,⁰ P. Gutjahr,²¹ C. Ha,⁵² A. Hallgren,⁶⁰ L. Halve,⁰ F. Halzen,³⁸ L. Hamacher,⁰ M. Handt,⁰ K. Hanson,³⁸ J. Hardin,¹³ A. A. Harnisch,²² P. Hatch,³¹ A. Haungs,²⁹ J. Häußler,⁰ K. Helbing,⁶¹ J. Hellrung,⁸ B. Henke,²² L. Hennig,²⁴ F. Henningsen,²⁴ L. Heuermann,⁰ R. Hewett,¹⁶ N. Heyer,⁶⁰ S. Hickford,⁶¹ A. Hidvegi,⁵³ C. Hill,²⁵ G. C. Hill,¹ R. Hmaid,¹⁴ K. D. Hoffman,¹⁷ A. Hollnagel,¹⁴ D. Hooper,³⁸ S. Hori,³⁸ K. Hoshina,^{38,c} M. Hostert,¹² W. Hou,²⁹ M. Hrywniak,⁵³ T. Huber,²⁹ K. Hultqvist,⁵³ K. Hyman,⁵⁶ A. Ishihara,¹⁴ W. Iwakiri,¹⁴ M. Jacquart,²⁰ S. Jain,³⁸ O. Janik,²⁴ M. Jansson,³⁵ M. Jin,¹² N. Kamp,¹² D. Kang,²⁹ W. Kang,⁴⁷ A. Kappes,⁴¹ L. Kardum,²¹ T. Karg,⁶² A. Karle,³⁸ A. Katil,²³ M. Kauer,³⁸ J. L. Kelley,³⁸ M. Khanal,⁵¹ A. Khatee Zathul,³⁸ A. Kheirandish,^{32,33} T. Kim,⁵⁵ H. Kimku,⁵² F. Kirchner,²⁴ J. Kiryluk,⁵⁴ C. Klein,⁶² S. R. Klein,^{5,6} Y. Kobayashi,¹⁴ S. Koch,²⁴ A. Kochocki,²² R. Koirala,⁴² H. Kolanoski,⁷ T. Kontrimas,²⁵ L. Köpke,³⁹ C. Kopper,²⁴ D. J. Koskinen,²⁰ P. Koundal,⁴² M. Kowalski,^{7,62} T. Kozynets,²⁰ A. Kravka,⁵¹ N. Krieger,⁸ T. Krishnan,¹² K. Kruiswijk,³⁵ E. Krupczak,²² A. Kumar,⁶² E. Kun,⁸ N. Kurahashi,⁴⁷ C. Lagunas Gualda,²⁵ L. Lallement Arnaud,⁹ M. J. Larson,¹⁷ F. Lauber,⁶¹ J. P. Lazar,³⁵ K. Leonard DeHolton,⁵⁹ A.

Leszczyńska,⁴² C. Li,³⁸ J. Liao,³ C. Lin,⁴² Q. R. Liu,¹¹ Y. T. Liu,⁵⁹ M. Liubarska,²³ C. Love,⁴⁷ L. Lu,³⁸ F. Lucarelli,²⁶ W. Luszczak,^{18,19} Y. Lyu,^{5,6} M. Macdonald,¹² E. Magnus,¹⁰ Y. Makino,³⁸ E. Manao,²⁵ S. Mancina,^{46,d} A. Mand,³⁸ I. C. Mariş,⁹ S. Marka,⁴⁴ Z. Marka,⁴⁴ L. Marten,⁰ I. Martinez-Soler,¹² R. Maruyama,⁴³ J. Mauro,³⁵ F. Mayhew,²² F. McNally,³⁶ K. Meagher,³⁸ A. Medina,¹⁹ M. Meier,¹⁴ Y. Merckx,¹⁰ L. Merten,⁸ S. Minji,⁵⁵ J. Mitchell,⁴ L. Molchany,⁴⁸ S. Mondal,⁵¹ T. Montaruli,²⁶ R. W. Moore,²³ Y. Morii,¹⁴ A. Mosbrugger,²⁴ D. Mousadi,⁶² E. Moyaux,³⁵ T. Mukherjee,²⁹ M. Nakos,³⁸ U. Naumann,⁶¹ R. Neshat,⁵¹ L. Neste,⁵³ M. Neumann,⁴¹ H. Niederhausen,²² M. U. Nisa,²² K. Noda,¹⁴ A. Noell,⁰ A. Novikov,⁴² A. Obertacke,⁵³ V. O'Dell,³⁸ A. Olivas,¹⁷ R. Orsoe,²⁵ J. Osborn,³⁸ E. O'Sullivan,⁶⁰ B. Owens,³¹ V. Palusova,³⁹ H. Pandya,⁴² A. Parenti,⁹ C. Parisel,³⁸ N. Park,³¹ V. Parrish,²² E. N. Paudel,⁵⁷ L. Paul,⁴⁸ C. Pérez de los Heros,⁶⁰ T. Pernice,⁶² T. C. Petersen,²⁰ J. Peterson,³⁸ S. Pick,⁶² M. Plum,⁴⁸ A. Pontén,⁶⁰ V. Poojyam,⁵⁷ B. Pries,²² R. Procter-Murphy,¹⁷ G. T. Przybylski,⁶ L. Pyras,⁵¹ C. Raab,³⁵ J. Rack-Helleis,³⁹ N. Rad,⁶² M. Ravn,⁶⁰ K. Rawlins,² Z. Rechav,³⁸ A. Rehman,⁴² I. Reistroffer,⁴⁸ E. Resconi,²⁵ C. D. Rho,⁵⁵ W. Rhode,²¹ L. Ricca,³⁵ B. Riedel,³⁸ A. Rifaie,⁶¹ E. J. Roberts,¹ S. Rodan,⁴⁹ M. Rongen,²⁴ A. Rosted,¹⁴ C. Rott,⁵¹ T. Ruhe,²¹ L. Ruohan,²⁵ D. Ryckbosch,²⁷ J. Saffer,³⁰ D. Salazar-Gallegos,²² P. Sampathkumar,²⁹ A. Sandrock,⁶¹ G. Sanger-Johnson,²² M. Santander,⁵⁷ S. Sarkar,⁴⁵ M. Scarnera,³⁵ M. Schaufel,⁰ H. Schieler,²⁹ S. Schindler,²⁴ L. Schlickmann,³⁹ B. Schlüter,⁴¹ F. Schlüter,⁹ N. Schmeisser,⁶¹ T. Schmidt,¹⁷ A. Scholz,²⁵ F. G. Schröder,^{29,42} S. Schwirn,⁰ S. Sclafani,¹⁷ D. Seckel,⁴² L. Seen,³⁸ M. Seikh,³⁴ S. Seunarine,⁴⁹ P. A. Sevre Myhr,³⁵ R. Shah,⁴⁷ S. Shah,⁵⁰ S. Shefali,³⁰ N. Shimizu,¹⁴ B. Skrzypek,⁵ R. Snihur,³⁸ J. Soedingrekso,²¹ D. Soldin,⁵¹ P. Soldin,⁰ G. Sommani,⁸ D. Song,⁹ C. Spannfellner,²⁵ G. M. Spiczak,⁴⁹ C. Spiering,⁶² J. Stachurska,²⁷ M. Stamatikos,¹⁹ T. Stanev,⁴² T. Stezelberger,⁶ T. Stürwald,⁶¹ T. Stuttard,²⁰ G. W. Sullivan,¹⁷ I. Taboada,³ S. Ter-Antonyan,⁴ A. Terliuk,²⁵ A. Thakuri,⁴⁸ M. Thiesmeyer,³⁸ W. G. Thompson,¹² J. Thwaites,³¹ S. Tilav,⁴² K. Tollefson,²² J. A. Torres,⁵¹ S. Toscano,⁹ D. Tosi,³⁸ K. Upshaw,⁴ A. Vaidyanathan,⁴⁰ N. Valtonen-Mattila,⁸ J. Valverde,⁴⁰ J. Vandenbroucke,³⁸ T. Van Eeden,⁶² N. van Eijndhoven,¹⁰ L. Van Rootselaar,²¹ J. van Santen,⁶² J. Vara,⁴¹ F. Varsi,³⁰ M. Velazquez,³ M. Venugopal,²⁹ M. Vereecken,²⁷ S. Vergara Carrasco,¹⁶ S. Verpoest,⁴² D. Veske,⁴⁴ A. Vijai,¹⁷ J. Villarreal,¹³ C. Walck,⁵³ A. Wang,³ E. H. S. Warrick,⁵⁷ C. Weaver,²² P. Weigel,¹³ A. Weindl,²⁹ J. Weldert,³⁹ A. Y. Wen,¹² C. Wendt,³⁸ J. Werthebach,²¹ M. Weyrauch,²⁹ N. Whitehorn,²² C. H. Wiebusch,⁰ D. R. Williams,⁵⁷ L. Witthaus,²¹ G. Wrede,²⁴ X. W. Xu,⁴ J. P. Yanez,²³ Y. Yao,³⁸ E. Yildizci,³⁸ S. Yoshida,¹⁴ F. Yu,¹² S. Yu,⁵¹ T. Yuan,³⁸ S. Yun-Cárcamo,⁴⁷ A. Zander Jurowitzki,²⁵ A. Zegarelli,⁸ S. Zhang,²² Z. Zhang,⁵⁴ P. Zhelnin,¹² P. Zilberman,³⁸ and C. Zilleruelo Cañas⁶²

⁰*III. Physikalisches Institut, RWTH Aachen University, D-52056 Aachen, Germany*

¹*Department of Physics, University of Adelaide, Adelaide, 5005, Australia*

²*Dept. of Physics and Astronomy, University of Alaska Anchorage, 3211 Providence Dr., Anchorage, AK 99508, USA*

³*School of Physics and Center for Relativistic Astrophysics, Georgia Institute of Technology, Atlanta, GA 30332, USA*

⁴*Dept. of Physics, Southern University, Baton Rouge, LA 70813, USA*

⁵*Dept. of Physics, University of California, Berkeley, CA 94720, USA*

- ⁶*Lawrence Berkeley National Laboratory, Berkeley, CA 94720, USA*
- ⁷*Institut für Physik, Humboldt-Universität zu Berlin, D-12489 Berlin, Germany*
- ⁸*Fakultät für Physik & Astronomie, Ruhr-Universität Bochum, D-44780 Bochum, Germany*
- ⁹*Université Libre de Bruxelles, Science Faculty CP230, B-1050 Brussels, Belgium*
- ¹⁰*Vrije Universiteit Brussel (VUB), Dienst ELEM, B-1050 Brussels, Belgium*
- ¹¹*Dept. of Physics, Simon Fraser University, Burnaby, BC V5A 1S6, Canada*
- ¹²*Department of Physics and Laboratory for Particle Physics and Cosmology, Harvard University, Cambridge, MA 02138, USA*
- ¹³*Dept. of Physics, Massachusetts Institute of Technology, Cambridge, MA 02139, USA*
- ¹⁴*Dept. of Physics and The International Center for Hadron Astrophysics, Chiba University, Chiba 263-8522, Japan*
- ¹⁵*Department of Physics, Loyola University Chicago, Chicago, IL 60660, USA*
- ¹⁶*Dept. of Physics and Astronomy, University of Canterbury, Private Bag 4800, Christchurch, New Zealand*
- ¹⁷*Dept. of Physics, University of Maryland, College Park, MD 20742, USA*
- ¹⁸*Dept. of Astronomy, Ohio State University, Columbus, OH 43210, USA*
- ¹⁹*Dept. of Physics and Center for Cosmology and Astro-Particle Physics, Ohio State University, Columbus, OH 43210, USA*
- ²⁰*Niels Bohr Institute, University of Copenhagen, DK-2100 Copenhagen, Denmark*
- ²¹*Dept. of Physics, TU Dortmund University, D-44221 Dortmund, Germany*
- ²²*Dept. of Physics and Astronomy, Michigan State University, East Lansing, MI 48824, USA*
- ²³*Dept. of Physics, University of Alberta, Edmonton, Alberta, T6G 2E1, Canada*
- ²⁴*Erlangen Centre for Astroparticle Physics, Friedrich-Alexander-Universität Erlangen-Nürnberg, D-91058 Erlangen, Germany*
- ²⁵*Physik-department, Technische Universität München, D-85748 Garching, Germany*
- ²⁶*Département de physique nucléaire et corpusculaire, Université de Genève, CH-1211 Genève, Switzerland*
- ²⁷*Dept. of Physics and Astronomy, University of Gent, B-9000 Gent, Belgium*
- ²⁸*Dept. of Physics and Astronomy, University of California, Irvine, CA 92697, USA*
- ²⁹*Karlsruhe Institute of Technology, Institute for Astroparticle Physics, D-76021 Karlsruhe, Germany*
- ³⁰*Karlsruhe Institute of Technology, Institute of Experimental Particle Physics, D-76021 Karlsruhe, Germany*
- ³¹*Dept. of Physics, Engineering Physics, and Astronomy, Queen's University, Kingston, ON K7L 3N6, Canada*
- ³²*Department of Physics & Astronomy, University of Nevada, Las Vegas, NV 89154, USA*
- ³³*Nevada Center for Astrophysics, University of Nevada, Las Vegas, NV 89154, USA*
- ³⁴*Dept. of Physics and Astronomy, University of Kansas, Lawrence, KS 66045, USA*
- ³⁵*UCLouvain, Centre for Cosmology, Particle Physics and Phenomenology, CP3, Chemin du Cyclotron 2, 1348 Louvain-la-Neuve, Belgium*
- ³⁶*Department of Physics, Mercer University, Macon, GA 31207-0001, USA*
- ³⁷*Dept. of Astronomy, University of Wisconsin—Madison, Madison, WI 53706, USA*
- ³⁸*Dept. of Physics and Wisconsin IceCube Particle Astrophysics Center, University of Wisconsin—Madison, Madison, WI 53706, USA*
- ³⁹*Institute of Physics, University of Mainz, Staudinger Weg 7, D-55099 Mainz, Germany*
- ⁴⁰*Department of Physics, Marquette University, Milwaukee, WI 53201, USA*
- ⁴¹*Institut für Kernphysik, Universität Münster, D-48149 Münster, Germany*
- ⁴²*Bartol Research Institute and Dept. of Physics and Astronomy, University of Delaware, Newark, DE 19716, USA*

- ⁴³*Dept. of Physics, Yale University, New Haven, CT 06520, USA*
- ⁴⁴*Columbia Astrophysics and Nevis Laboratories, Columbia University, New York, NY 10027, USA*
- ⁴⁵*Dept. of Physics, University of Oxford, Parks Road, Oxford OX1 3PU, United Kingdom*
- ⁴⁶*Dipartimento di Fisica e Astronomia Galileo Galilei, Università Degli Studi di Padova, I-35122 Padova PD, Italy*
- ⁴⁷*Dept. of Physics, Drexel University, 3141 Chestnut Street, Philadelphia, PA 19104, USA*
- ⁴⁸*Physics Department, South Dakota School of Mines and Technology, Rapid City, SD 57701, USA*
- ⁴⁹*Dept. of Physics, University of Wisconsin, River Falls, WI 54022, USA*
- ⁵⁰*Dept. of Physics and Astronomy, University of Rochester, Rochester, NY 14627, USA*
- ⁵¹*Department of Physics and Astronomy, University of Utah, Salt Lake City, UT 84112, USA*
- ⁵²*Dept. of Physics, Chung-Ang University, Seoul 06974, Republic of Korea*
- ⁵³*Oskar Klein Centre and Dept. of Physics, Stockholm University, SE-10691 Stockholm, Sweden*
- ⁵⁴*Dept. of Physics and Astronomy, Stony Brook University, Stony Brook, NY 11794-3800, USA*
- ⁵⁵*Dept. of Physics, Sungkyunkwan University, Suwon 16419, Republic of Korea*
- ⁵⁶*Institute of Physics, Academia Sinica, Taipei, 11529, Taiwan*
- ⁵⁷*Dept. of Physics and Astronomy, University of Alabama, Tuscaloosa, AL 35487, USA*
- ⁵⁸*Dept. of Astronomy and Astrophysics, Pennsylvania State University, University Park, PA 16802, USA*
- ⁵⁹*Dept. of Physics, Pennsylvania State University, University Park, PA 16802, USA*
- ⁶⁰*Dept. of Physics and Astronomy, Uppsala University, Box 516, SE-75120 Uppsala, Sweden*
- ⁶¹*Dept. of Physics, University of Wuppertal, D-42119 Wuppertal, Germany*
- ⁶²*Deutsches Elektronen-Synchrotron DESY, Platanenallee 6, D-15738 Zeuthen, Germany*
- ^a*also at Department of Space, Earth and Environment, Chalmers University of Technology, 412 96 Gothenburg, Sweden*
- ^b*also at INFN Padova, I-35131 Padova, Italy*
- ^c*also at Earthquake Research Institute, University of Tokyo, Bunkyo, Tokyo 113-0032, Japan*
- ^d*now at INFN Padova, I-35131 Padova, Italy*

ABSTRACT: The IceCube Neutrino Observatory, a cubic-kilometer detector at the South Pole, identifies neutrino flavor through event morphology. Sparse photon detection makes this classification particularly challenging in the 5–100 GeV regime, the energy range relevant for oscillation measurements and searches for physics beyond the Standard Model. We introduce WavePID, a template-based log-likelihood-ratio classifier that exploits nanosecond-scale timing on individual detector modules through three observables: the distance to the reconstructed vertex, the early-charge fraction, and the module-to-module time difference. Evaluated on a cascade-enriched sample selected by a state-of-the-art graph neural network, WavePID improves both cascade purity and classification performance over the neural network alone. This demonstrates that per-module pulse timing carries flavor-identification information complementary to morphology-based classifiers, opening a new physics-motivated observable for low-energy neutrino reconstruction. Geant4 simulations associate this signal with differences in Cherenkov emission geometry between muon tracks and electromagnetic showers. These results motivate exploiting nanosecond-scale pulse timing in future low-energy classifiers and in detector designs with improved per-module timing in next-generation neutrino telescopes.

KEYWORDS: Neutrino flavors, Statistical methods, Particle identification, Physics-motivated observables, Cherenkov detectors

Contents

1	Introduction	1
1.1	The IceCube Detector	1
1.2	The challenge of low-energy flavor identification	2
2	The origin of photon hits on DOMs	3
2.1	Geant4 simulation setup	3
2.2	Photon arrival time distributions	4
3	The WavePID algorithm	6
4	WavePID in IceCube	7
4.1	Pulse timing on individual IceCube DOMs	7
4.2	Test statistic performance and systematics	8
5	Conclusion and outlook	11
A	Supplemental Material	S1

1 Introduction

1.1 The IceCube Detector

The IceCube Neutrino Observatory [1] is a cubic-kilometer neutrino detector instrumented with optical sensors called Digital Optical Modules (DOMs) embedded in the deep, glacial ice at the geographic South Pole. It features a densely instrumented sub-array, DeepCore, designed for low-energy event reconstruction, extending IceCube’s sensitivity down to several GeV [2]. This extended energy range enables precision measurements of atmospheric oscillation parameters and searches for physics beyond the Standard Model [2–5]. Flavor separation is central to this scientific case, and it is the primary focus of the method that we introduce in this article.

Neutrino interactions in or near the instrumented volume produce charged secondaries that emit Cherenkov photons, which propagate through the ice and are detected by the DOMs. Depending on the final-state particle content, two distinct event morphologies are defined. *Track* events arise when a relativistic muon traverses the detector, producing an elongated light pattern. This morphology is associated primarily with charged-current (CC) ν_μ interactions and, less frequently, CC ν_τ interactions in which the τ decays to a μ and neutrinos. *Cascade* events correspond to localized, approximately isotropic light depositions from CC ν_e and ν_τ interactions and neutral-current interactions of all flavors. Track–cascade separation enters atmospheric mixing analyses [3, 6], the neutrino mass ordering [4], ν_τ appearance [7], and sterile neutrino searches [5]. Misclassified events migrate between flavor channels and inflate the uncertainties on the extracted parameters.

For detection, each DOM houses a photomultiplier tube (PMT) that records time-resolved waveforms. Pulses read out by the Analog Transient Waveform Digitizer (ATWD) are sampled in 128 bins of 3.3 ns width, providing nanosecond-level timing information. Calibrated pulse series are extracted from the recorded waveforms by deconvolution of a single photoelectron template [1].

1.2 The challenge of low-energy flavor identification

Dim events with sparse light detection are common in the 5–100 GeV range, the low-energy end of IceCube’s GeV–PeV sensitivity, posing the classification challenge this study addresses. The event-level hit multiplicity n_{hit} is the number of DOMs recording at least one pulse after noise cleaning [8]. This study focuses on the regime $10 \leq n_{\text{hit}} < 20$, chosen because (i) it contains over half of detected low-energy neutrino events in IceCube DeepCore MC; (ii) it aligns with the standard low-energy event selection used in oscillation analyses; and (iii) it is the regime where timing-based methods offer the largest relative gain, because the light pattern weakly constrains the event morphology, as illustrated in fig. 1.

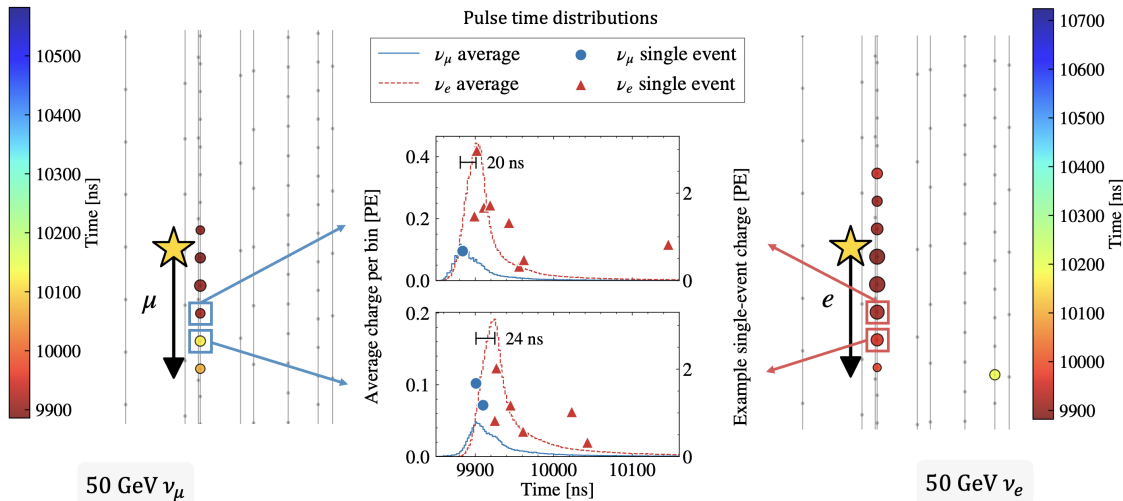


Figure 1: Neutrino event signatures: 50 GeV ν_μ CC (left) and ν_e CC (right) interactions, with 35 GeV deposited by the charged lepton and 15 GeV by hadrons. A star marks the neutrino interaction vertex, sphere size encodes charge, and color encodes timing. At this hit multiplicity (13 for ν_μ , 18 for ν_e), the morphology provides limited discrimination. The center panel shows pulse time distributions from 10^5 photon propagations for two selected DOMs, with horizontal bars marking the peak separation that WavePID exploits. Example pulse series are overlaid as markers.

State-of-the-art low-energy classification in IceCube uses graph neural networks (GNNs) such as DynEdge [9]. While this particle identification (PID) method performs well for events with many hits, the achievable separation power decreases sharply at lower hit multiplicities, motivating a more effective use of fine-grained timing information. Next-generation neutrino telescopes increasingly build improved per-module timing into the optical-module architecture by design [10–14], replacing the single large photomultiplier per module with smaller multi-PMT arrays or silicon photomultipliers and faster digitization. This is especially powerful in water, where the longer

scattering length preserves the fine timing structure at the sensor. The central question of this work is whether nanosecond-scale timing on individual DOMs carries PID information that existing classifiers do not capture. Because a muon track produces a sharp, direct Cherenkov front while an electromagnetic cascade builds up its light from secondaries over several nanoseconds (cf. section 2), the discriminating structure is concentrated in a brief $O(10\text{ ns})$ window following the first pulse on each DOM. Although DynEdge ingests the raw per-pulse information (DOM position, time, and charge) as node features and learns its own representation from it, the pulse timestamps are normalized to the $O(\mu\text{s})$ event duration, which may compress this early-time structure into a small fraction of the node feature range. WavePID, on the other hand, operates on per-DOM pulse series data and explicitly targets the relative charge accumulation within the first several nanoseconds.

This early-time regime is motivated by the demonstrated performance of waveform-based PID in single PMTs in controlled water Cherenkov measurements. Specifically, in the Fermilab FNAL-1267 test-beam study [15], pulse-shape information from a single PMT was used to separate minimum ionizing pions from radiative electrons in the several-GeV regime. The work presented here tests whether the discrimination demonstrated at Fermilab transfers to IceCube, representing—to our knowledge—the first explicit use of single-DOM nanosecond-scale timing information for PID in a neutrino telescope.

The remainder of this article is organized as follows. Section 2 presents Geant4 photon arrival-time studies investigating the underlying microphysics and motivating the timing observables. Section 3 introduces WavePID as a compact classifier that exploits pulse timing on the order of ten nanoseconds as an additional classification dimension, complementing existing morphology-based methods in the low-hit regime. Section 4 evaluates its performance and systematics on IceCube DeepCore MC in the sparse target regime $n_{\text{hit}} \in [10, 20)$, and section 5 concludes.

2 The origin of photon hits on DOMs

To study the microphysics origin of timing differences between tracks and cascades, we simulate photon arrival time distributions (PATDs) on a single DOM in ice using Geant4 [16]. Charged particles are injected at fixed energy and impact parameter (the perpendicular distance between the particle trajectory and the DOM). This isolates the primary light deposition mechanisms that underlie this PID technique to focus on the microphysics interpretation, though it does not include the full PMT response or detector chain, which is addressed in section 4.

2.1 Geant4 simulation setup

Using Geant4 and the IceCube OMSim framework [17], we simulate photon hits on a single DOM in ice according to the SPICE model [18]. Primary muons and electrons are injected at 5–100 GeV and results are shown for 10, 50, and 80 GeV, representative of the full range. Geant4 propagates each particle and its secondaries, generates Cherenkov photons, and transports them through ice including scattering and absorption. Fig. 2 shows Geant4 renderings of 50 GeV electrons and muons injected into ice in the single-DOM setup, including the secondary particles they produce. The different locations of charged particles shown in fig. 2 for muons and electrons already provide qualitative hints for the different PATDs discussed in section 2.2. We also record how each photon was created to investigate the origin of the PATD shapes.

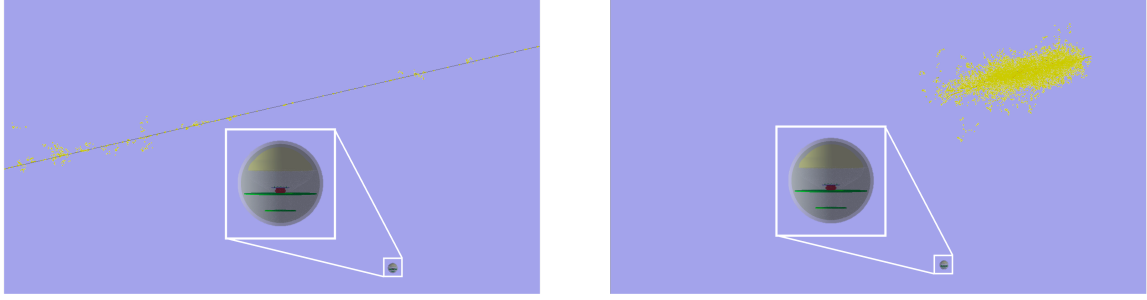


Figure 2: Geant4 OMSim event display of a 50 GeV muon (left) and electron (right) passing by a DOM. The white rectangle zooms in on the DOM. Yellow points indicate the sampled trajectory steps of the charged particles (injected lepton and secondaries), Cherenkov photons are not shown.

2.2 Photon arrival time distributions

The timing residual is defined as the difference between the observed photon arrival time and the expectation for unscattered Cherenkov light given the source–DOM geometry, and forms the x-axis of fig. 3. The muon PATD develops faster and is concentrated at early residual times, while the cascade PATD is broader. This difference follows from the light-production mechanism. Muon light is dominated by direct Cherenkov emission, whereas cascade light is dominated by Bremsstrahlung secondaries that are produced as the electromagnetic shower develops, spreading out the arrival times. The decompositions by photon origin in fig. 3 make this explicit. The *primary particle* label denotes direct Cherenkov light from the injected particle. *Primary-induced secondaries* denotes light from particles produced in its electromagnetic interactions, such as δ rays from ionization. *Bremsstrahlung secondaries* denotes light from e^+e^- pairs produced by Bremsstrahlung photons radiated in the shower. The lower per-DOM photon yield for muons is geometric. A 50 GeV muon emits Cherenkov light over more than 200 m of ice, while a 50 GeV electron-induced shower is compact enough that nearby DOMs see most of it. Across the 5–100 GeV range, muons behave as minimum ionizing particles (MIPs) and this picture is qualitatively stable, motivating the use of early-time pulse structure as a PID observable.

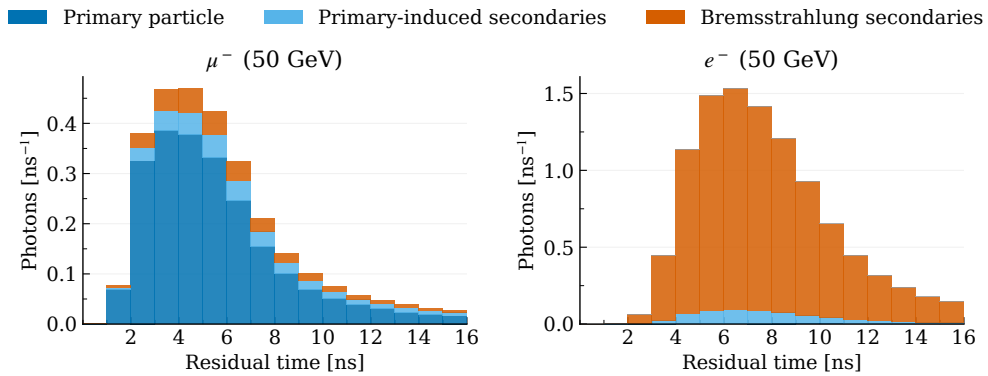


Figure 3: Average photon arrival time distribution for 50 GeV muons (left) and electrons (right) at 20 m impact parameter. Muon events are dominated by direct Cherenkov emission from the primary track, while electron events are dominated by Bremsstrahlung secondaries.

A useful derived observable is the *early-photon fraction*, defined as the fraction of photons arriving within a short window Δt after the first photon. Fig. 4 shows this fraction as a function of the impact parameter for three energies and two integration windows.

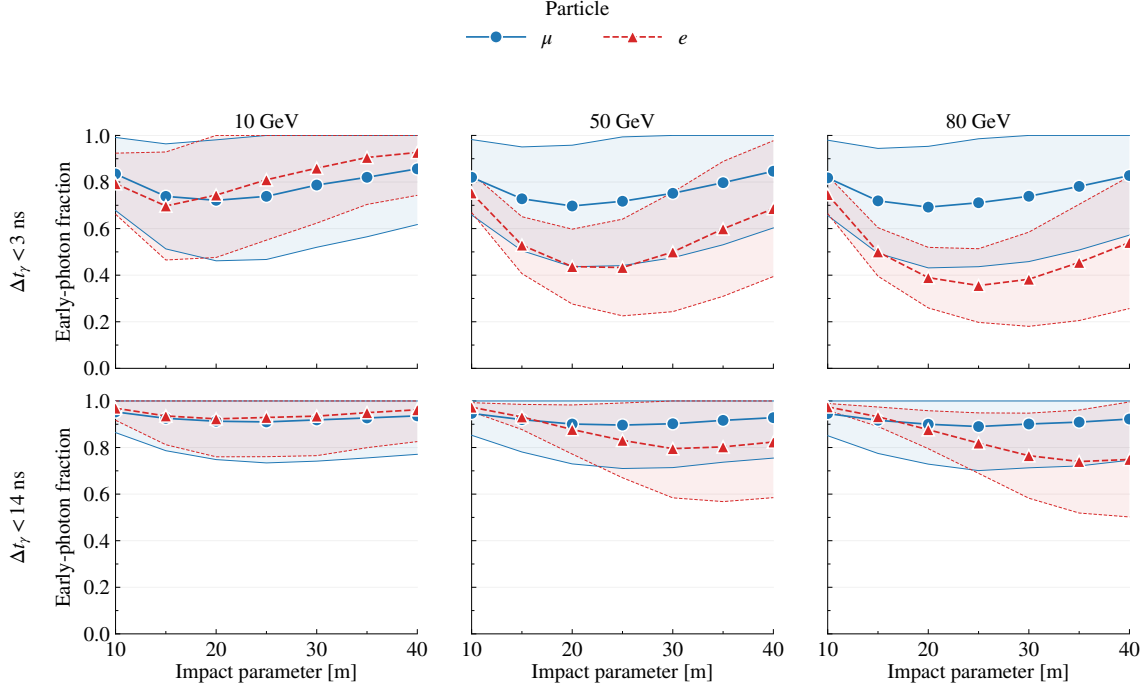


Figure 4: Early-photon fraction (within Δt of the first photon) as a function of impact parameter, for muons (blue) and electrons (red). Panels span three particle energies (10, 50, 80 GeV) and two integration windows ($\Delta t = 3, 14$ ns). Shaded regions indicate one standard deviation between events. The 3 ns window illustrates the discrimination available at the photon level with high timing resolution, while the 14 ns window matches the timing adopted by WavePID (cf. section 3).

To isolate the microphysics origin of track-cascade differences, the Geant4 study in this section evaluates early-photon fractions with integration windows as short as 3 ns, finer than the timing aggregation used on reconstructed IceCube pulses. At the 3 ns window, the separation in ice reproduces that of the FNAL-1267 water Cherenkov study [15]. The 14 ns window provides a detector-relevant aggregation scale for comparison with the reconstructed-pulse implementation in section 3. At 50 and 80 GeV with the 3 ns window, the separation is robust across impact parameters and peaks at 15–30 m. Broadening the time window to 14 ns reduces the separation at impact parameters below ~ 20 m, where the characteristic Cherenkov peak from tracks is no longer resolved. At 10 GeV the early-photon fraction loses its separating power at the 14 ns window.

These photon-level trends apply to a single per-DOM observable in isolation. WavePID combines the early-charge fraction with the DOM-to-vertex distance and the inter-module time difference in a multivariate template (section 3), and the detector-level classifier performance across the full 5–100 GeV range is evaluated in section 4.2.

3 The WavePID algorithm

This section presents the WavePID algorithm and its application to IceCube. The objective is to test whether the early-time signal identified in section 2 provides classification power beyond existing methods. To this end, WavePID is constructed as a compact log-likelihood ratio over three physics-motivated observables, defined in table 1. If this approach yields discrimination that a state-of-the-art GNN does not capture, the information content of the timing channel is indicated. While WavePID is constructed without explicit dependence on hit multiplicity and can be applied across a broad energy range, this study focuses on the low-hit regime ($n_{\text{hit}} < 20$) where morphology-based classification is most limited and timing-based approaches offer the largest relative improvement.

WavePID’s per-DOM observables. WavePID operates on nanosecond-resolution ATWD pulses from individual DOMs, represented as an ordered set of reconstructed pulses $\{(t_p, q_p)\}$ with timestamps t_p and charges q_p . Only pulses digitized by the ATWD are considered. For each DOM n , the algorithm constructs a feature vector \mathbf{x}_n from the three observables defined in table 1:

$$\mathbf{x}_n = (r_n, \xi_n^t, \Delta t_n). \quad (3.1)$$

Table 1: Per-DOM observables used by WavePID.

Symbol	Description
r_n	Distance from DOM n to reconstructed interaction vertex; captures distance-dependent timing structure
ξ_n^t	Fraction of charge on DOM n arriving within first t ns; sensitive to early-time Cherenkov emission
Δt_n	Time of first pulse on DOM n relative to the earliest pulse on any DOM; encodes event-wide timing

Template construction. The feature space $(r, \xi^t, \Delta t)$ is discretized into three-dimensional bins $\{\mathcal{B}_{ijk}\}$. For an event e , the occupancy tensor

$$H_{ijk}^e = \sum_{n \in e} \mathbb{I}[\mathbf{x}_n \in \mathcal{B}_{ijk}], \quad (3.2)$$

counts the number of DOMs whose features fall into bin \mathcal{B}_{ijk} . This results in a 3D histogram of the DOMs in the feature space. Shape-only templates λ_{ijk}^s are constructed from labeled MC simulations for each hypothesis $s \in \{\text{cascade}, \text{track}\}$. Let \mathcal{E}_s denote the set of MC events with true label s . Weighted bin counts are accumulated as weighted 3D histograms

$$N_{ijk}^s = \sum_{e \in \mathcal{E}_s} w^e \cdot H_{ijk}^e, \quad W^s = \sum_{e \in \mathcal{E}_s} w^e, \quad (3.3)$$

where w^e is the per-event weight [19], inherited by each DOM, N_{ijk}^s is the weighted DOM count in bin \mathcal{B}_{ijk} for class s , and W^s is the total weight of class s . To ensure numerical stability, a small

floor $\varepsilon_\lambda > 0$ is applied before normalizing to obtain proper shape-only probability mass functions:

$$\lambda_{ijk}^s = \frac{\tilde{\lambda}_{ijk}^s}{\sum_{i',j',k'} \tilde{\lambda}_{i',j',k'}^s}, \quad \text{with} \quad \tilde{\lambda}_{ijk}^s = \max\left(\varepsilon_\lambda, \frac{N_{ijk}^s}{W^s}\right). \quad (3.4)$$

The floor is set to $\varepsilon_\lambda = 10^{-12}$. Note that $\sum_{ijk} \tilde{\lambda}_{ijk}^s$ gives the average number of hits in an event of class s up to the effect of this floor.

Test statistic. To discriminate between track and cascade morphologies, WavePID employs a binned log-likelihood ratio. Assuming independent Poisson-distributed bin occupancies with expected bin occupancy μ_{ijk}^s under hypothesis s , the likelihood for hypothesis s for an event e is

$$\mathcal{L}_s(e) = \prod_{i,j,k} \text{Pois}(H_{ijk}^e | \mu_{ijk}^s) = \prod_{i,j,k} \frac{e^{-\mu_{ijk}^s} (\mu_{ijk}^s)^{H_{ijk}^e}}{H_{ijk}^e!}, \quad (3.5)$$

where $\mu_{ijk}^s \propto \lambda_{ijk}^s$ and μ_{ijk}^s is normalized to the number of hits in an event e , i.e., $\sum_{ijk} \mu_{ijk}^s = \sum_{ijk} H_{ijk}^e$. The test statistic (TS) is defined as the shape-only log-likelihood ratio

$$\text{TS}_e = \log \frac{\mathcal{L}_e^{\text{cascade}}}{\mathcal{L}_e^{\text{track}}} = \sum_{i,j,k} H_{ijk}^e \log \frac{\lambda_{ijk}^{\text{cascade}}}{\lambda_{ijk}^{\text{track}}}, \quad (3.6)$$

representing a sum over bins of the per-bin log-odds, each weighted by the observed hits H_{ijk}^e . By construction, larger values of TS correspond to more cascade-like events. As the test statistic reduces to a lookup and summation over DOM feature bins, WavePID is computationally inexpensive.

4 WavePID in IceCube

This section evaluates WavePID performance on a set of 31 IceCube MC ensembles that represent the dominant detector and ice-model uncertainties, including DOM efficiency, the optical properties of the refrozen ice in the drill holes immediately surrounding each string (hole ice), and the scattering and absorption of the surrounding glacial ice (bulk ice) [18].

4.1 Pulse timing on individual IceCube DOMs

To examine whether the timing differences identified in the Geant4 study persist through the full detector simulation chain, we use one representative 50 GeV ν_μ event and one representative 50 GeV ν_e event. These events are chosen to represent typical deep-inelastic-scattering interactions, which dominate the studied energy range. The interaction vertex, directions, and the lepton and hadronic energy deposition are all held fixed. We resample the stochastic photon propagation and PMT response and then apply the standard pulse extraction and DeepCore processing 10^5 times, yielding the same cleaned pulses used by WavePID. This isolates the detector-chain variability for a fixed event, without folding in event-to-event physics fluctuations. The full per-event complexity is present in the WavePID evaluation on the complete MC sample, presented in section 4.2. Fig. 5 shows that the early-charge fraction retains discriminating power in this geometry after the complete simulation chain, indicating that the signal survives the detector response.

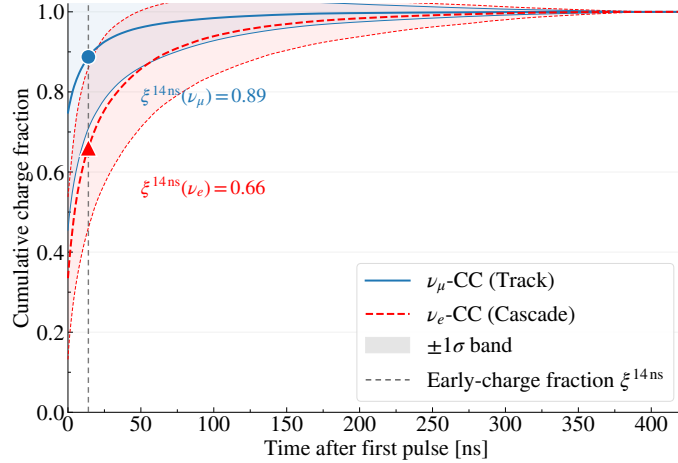


Figure 5: Cumulative charge fraction distribution for ν_μ and ν_e charged-current interactions at 50 GeV neutrino energy with 35 GeV deposited by the charged lepton and 15 GeV by hadrons. Results are shown for a single DeepCore DOM and one representative event geometry. Shaded regions indicate one standard deviation across 10^5 repetitions of the photon propagation, PMT response, and detector processing. The vertical dashed line marks 14 ns, which is defined as the early-charge fraction time window in section 4.2.

This motivates compiling the per-DOM observables into the binned templates described in section 3. The WavePID test statistic is then obtained by summing the bin-wise log-odds over all contributing DOMs in an event, as evaluated below.

4.2 Test statistic performance and systematics

We present the implementation and performance of WavePID on IceCube DeepCore. The study uses the oscNext event selection [9, 20], which provides a high-purity selection of neutrino events in the 5–100 GeV range with atmospheric muon contamination below 1%. The MC-truth particle and interaction type are used for the construction of the TS templates, where ν_μ CC interactions are defined as tracks and all other neutrino interactions as cascades. The simulation used here relies on GENIE v2.12.8 [19], which does not include Meson Exchange Current (MEC). MEC will mainly impact the amount of energy given to the outgoing lepton and hadron, which can in principle change the expected light yield of low energy tracks and cascades. We leave detailed evaluation of the impact of MEC on WavePID to future work. We restrict the sample to the cascade-PID bin of the oscNext selection, defined by a DynEdge-PID score ≤ 0.4 , where lower values correspond to more cascade-like events. We further require $10 \leq n_{\text{hit}} < 20$, focusing on the target regime of this method where morphology-based classification is weakest.

Reconstruction and binning. WavePID’s DOM-vertex distance r is computed using the interaction vertex reconstructed by DynEdge. The bin edges used in this study are

$$\begin{aligned}
 \mathbf{e}_r &= (0, 35, 50, 65, 84, 111, 1500) \text{ m}, \\
 \mathbf{e}_\xi &= (0.0, 0.1, 0.2, \dots, 0.9, 1.0), \\
 \mathbf{e}_{\Delta t} &= (0, 5, 36, 253, 1800) \text{ ns},
 \end{aligned} \tag{4.1}$$

where the distance bins in \mathbf{e}_r are defined by quantiles of the distance distribution over the full MC sample, the early-charge fraction ξ^t is binned uniformly on $[0, 1]$ for $t = 14$ ns, and the Δt bins are log-spaced from 5 to 1800 ns, with a separate first bin $[0, 5)$ ns added to isolate the earliest pulses. The vertex resolution of 10–15 m [9] is the dominant contribution to the uncertainty on r , exceeding the ~ 1 m uncertainty on DOM positions [21]. A dedicated check confirms that adding a Gaussian smearing of $\sigma = 10$ m per axis to the reconstructed vertex leaves the area under the receiver-operating-characteristic (ROC) curve (AUC) stable to within ~ 0.02 , consistent with the chosen distance binning being coarse relative to the DynEdge vertex resolution. The 14 ns time window is large compared to both the PMT transit time spread (~ 3.2 ns [22]) and the timing accuracy of the Reciprocal Active Pulsing (RapCal) calibration system (~ 1.2 ns [1]), indicating that instrumental timing uncertainties are subdominant to the physical timing differences exploited by the early-charge fraction. The bin edges and time window were optimized empirically for PID performance in events with 10–20 hits, informed by the distance and timing dependencies identified in section 2. Hyperparameters were fixed on the training set prior to evaluation on the test set.

Performance and benchmarking. The cascade and track templates for WavePID are constructed from an independent 80% training set and all WavePID and DynEdge ROC curves are evaluated on the held-out 20% test set. Both classifiers are benchmarked within the DynEdge-selected cascade sample, so the reported AUCs measure residual flavor-separation power after the GNN pre-selection.

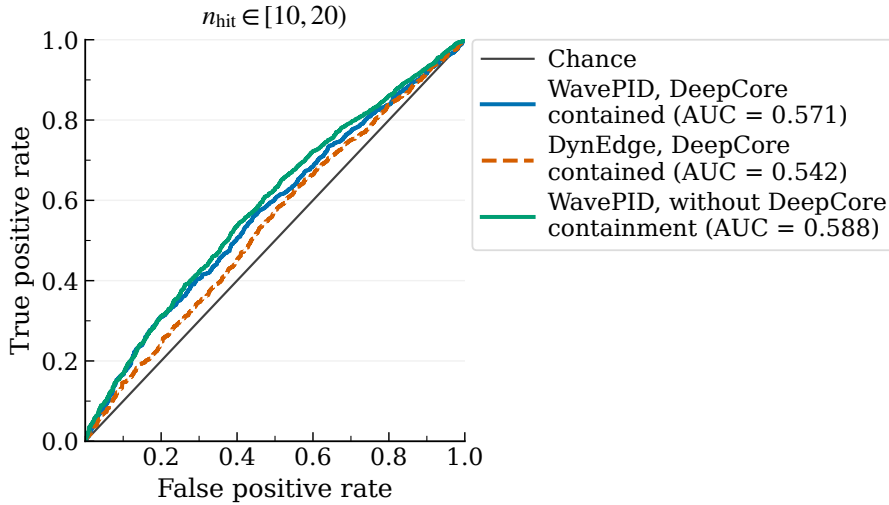


Figure 6: PID performance evaluated on a held-out 20% test set, for cascade classification in the DynEdge cascade PID bin with $n_{\text{hit}} \in [10, 20)$. WavePID (blue, solid) achieves higher AUC than DynEdge (orange, dashed) within the standard DeepCore-contained event selection. Relaxing the DeepCore containment requirement (green, solid) slightly increases separation power, as WavePID does not rely on the containment cut and benefits from the larger sample.

As shown in fig. 6, for $10 \leq n_{\text{hit}} < 20$, WavePID achieves higher AUC than DynEdge (0.57 vs. 0.54) despite relying on only three observables, demonstrating that early-time pulse structure encodes PID information not captured by the GNN. Both ROC curves are evaluated within the DynEdge cascade PID bin and sweep each classifier’s threshold across the score range available

in that sub-sample, so they span the full $[0, 1]$ true positive rate and false positive rate range by construction. The DynEdge AUC reflects the residual ordering power of the DynEdge score within its own cascade bin, with most of DynEdge’s separating power having been used by the upstream cut at DynEdge-PID ≤ 0.4 . For larger hit multiplicities, DynEdge achieves higher AUC, consistent with its ability to exploit richer topological information, confirming that the two methods access complementary features. The AUC margin itself is secondary to this complementarity, positioning WavePID as an additional classification dimension rather than a standalone alternative to morphology-based methods.

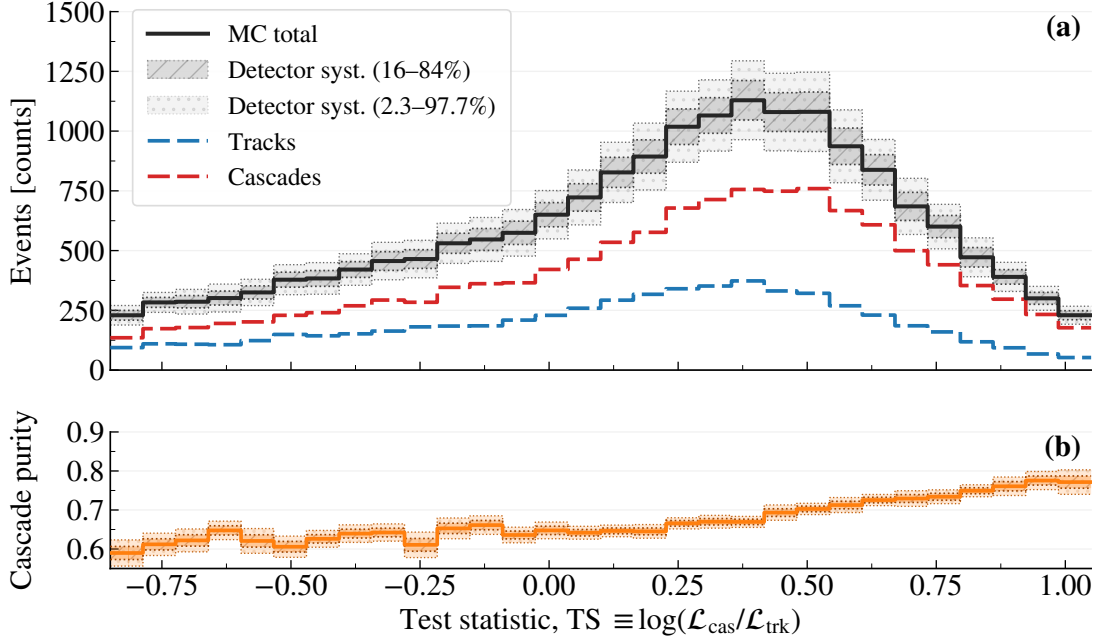


Figure 7: Top panel (a): WavePID test statistic distribution in the DynEdge cascade PID bin for simulated true tracks (ν_μ CC) and cascades (all other neutrino interactions), computed as the shape-only log-likelihood ratio. The shaded bands indicate the 16–84th and the 2.3–97.7th percentile variation across 31 detector-systematics MC sets. Lower panel (b): cascade purity.

Systematics. The WavePID template is constructed only once from the nominal MC set and evaluated on all 31 oscNext detector-systematic ensembles, which sample DOM efficiency, hole-ice parameters, and bulk-ice optical properties. The resulting spread is shown as shaded bands in fig. 7, where the TS shape and track–cascade separation remain stable across all configurations. A full treatment of physics-parameter uncertainties and additional detector effects is left for dedicated physics analyses, as discussed in section 5.

Purity increase. Applying a threshold $TS > TS_{\text{cut}}$ to the WavePID output increases the cascade purity P^C within the DynEdge cascade selection. At a representative operating point retaining 20% of cascades, the baseline purity from DynEdge of $P_0^C = 0.66$ increases to $P^C = 0.75$ for the nominal MC set. Beyond the nominal set, across the 31 detector-systematic ensembles, the purity gain is $+7\% \pm 1\%$, indicating robustness to the dominant detector uncertainties. The 20% operating point

is illustrative rather than prescriptive. A hard cut at this operating point keeps only whether each event passes the threshold and discards the continuous per-event score. In a physics analysis the test statistic or the early-charge fraction is more useful as an additional input variable. Quantification of the resulting physics impact is left to dedicated follow-up studies (section 5).

5 Conclusion and outlook

We presented WavePID, a compact template-based classifier that exploits nanosecond-scale pulse timing for flavor identification in IceCube DeepCore at 5–100 GeV. We demonstrate nanosecond-scale Cherenkov timing at individual DOMs as a previously unexploited, first-principles-motivated information channel for flavor identification in neutrino telescopes.

Waveform-based PID with single PMTs has previously been demonstrated in controlled beam measurements [15], and here we show that the same timing structure remains effective after propagation through South Pole ice and digitization by IceCube DOMs, with discrimination concentrated in the regime where the primary lepton’s leading, minimally scattered Cherenkov front is resolved by per-DOM pulse timing. Using only three physics-motivated observables (DOM-to-vertex distance, early-charge fraction, and inter-module time difference), WavePID achieves higher AUC than DynEdge within the DynEdge-selected cascade sample in the low-hit regime ($10 \leq n_{\text{hit}} < 20$). A microphysics interpretation is provided by Geant4 photon arrival-time studies, which associate the observed discrimination with differences in Cherenkov emission geometry between muon tracks and electromagnetic showers. These results show that early nanosecond-scale timing carries discriminating information beyond that captured by the existing event-level classifier in this regime, with WavePID’s three physics-motivated observables complementary to the learned representation that DynEdge builds from the raw pulses.

The configuration presented here defines a baseline implementation, and the optimal choice of observables, binning, and operating point depends on the physics target. In practice, the natural application of WavePID is as an additional classification dimension, where the test statistic, or the early-charge fraction alone, can be combined with the score of a classifier like DynEdge-PID in a multi-dimensional selection or used as an input to a likelihood fit, retaining the full event sample while exploiting per-event timing information.

Application to IceCube data and quantification of the corresponding physics impact are left to dedicated follow-up studies. Extensions such as electromagnetic versus hadronic cascade separation are natural next steps. More broadly, WavePID motivates the development of fine-grained per-module timing in next-generation neutrino telescopes operating in ice or water, such as the IceCube Upgrade [23] and IceCube-Gen2 [14], KM3NeT/ORCA [10, 24], P-ONE [12], TRIDENT [11], and HUNT [13], particularly for detectors with multi-PMT or hybrid optical modules where per-module timing is optimized by design.

Acknowledgments

The IceCube collaboration acknowledges the significant contributions to this manuscript from Steven Young Eulig. The authors gratefully acknowledge the support from the following agencies and institutions: USA – U.S. National Science Foundation-Office of Polar Programs, U.S. National

Science Foundation-Physics Division, U.S. National Science Foundation-EPSCoR, U.S. National Science Foundation-Office of Advanced Cyberinfrastructure, Wisconsin Alumni Research Foundation, Center for High Throughput Computing (CHTC) at the University of Wisconsin–Madison, Open Science Grid (OSG), Partnership to Advance Throughput Computing (PATH), Advanced Cyberinfrastructure Coordination Ecosystem: Services & Support (ACCESS), Frontera and Ranch computing project at the Texas Advanced Computing Center, U.S. Department of Energy-National Energy Research Scientific Computing Center, Particle astrophysics research computing center at the University of Maryland, Michigan State University, Astroparticle physics computational facility at Marquette University, NVIDIA Corporation, and Google Cloud Platform; Belgium – Funds for Scientific Research (FRS-FNRS and FWO), FWO Odysseus and Big Science programmes, and Belgian Federal Science Policy Office (Belspo); Germany – Bundesministerium für Forschung, Technologie und Raumfahrt (BMFTR), Deutsche Forschungsgemeinschaft (DFG), Helmholtz Alliance for Astroparticle Physics (HAP), Initiative and Networking Fund of the Helmholtz Association, Deutsches Elektronen Synchrotron (DESY), and High Performance Computing cluster of the RWTH Aachen; Sweden – Swedish Research Council, Swedish Polar Research Secretariat, Swedish National Infrastructure for Computing (SNIC), and Knut and Alice Wallenberg Foundation; European Union – EGI Advanced Computing for research; Australia – Australian Research Council; Canada – Natural Sciences and Engineering Research Council of Canada, Calcul Québec, Compute Ontario, Canada Foundation for Innovation, WestGrid, and Digital Research Alliance of Canada; Denmark – Villum Fonden, Carlsberg Foundation, and European Commission; New Zealand – Marsden Fund; Japan – Japan Society for Promotion of Science (JSPS), Ministry of Education, Culture, Sports, Science and Technology (MEXT), and Institute for Global Prominent Research (IGPR) of Chiba University; Korea – National Research Foundation of Korea (NRF); Switzerland – Swiss National Science Foundation (SNSF).

References

- [1] ICECUBE collaboration, *The IceCube neutrino observatory: Instrumentation and online systems*, *JINST* **12** (2017) P03012 [[1612.05093](#)].
- [2] ICECUBE collaboration, *The Design and Performance of IceCube DeepCore*, *Astropart. Phys.* **35** (2012) 615 [[1109.6096](#)].
- [3] ICECUBE collaboration, *Measurement of atmospheric neutrino mixing with improved IceCube DeepCore calibration and data processing*, *Phys. Rev. D* **108** (2023) 012014 [[2304.12236](#)].
- [4] ICECUBE collaboration, *Development of an analysis to probe the neutrino mass ordering with atmospheric neutrinos using three years of IceCube DeepCore data*, *Eur. Phys. J. C* **80** (2020) 9 [[1902.07771](#)].
- [5] ICECUBE collaboration, *Search for a light sterile neutrino with 7.5 years of IceCube DeepCore data*, *Phys. Rev. D* **110** (2024) 072007 [[2407.01314](#)].
- [6] ICECUBE collaboration, *Measurement of Atmospheric Neutrino Oscillation Parameters Using Convolutional Neural Networks with 9.3 Years of Data in IceCube DeepCore*, *Phys. Rev. Lett.* **134** (2025) 091801 [[2405.02163](#)].
- [7] ICECUBE collaboration, *Measurement of Atmospheric Tau Neutrino Appearance with IceCube DeepCore*, *Phys. Rev. D* **99** (2019) 032007 [[1901.05366](#)].

- [8] ICECUBE collaboration, *Low energy event reconstruction in IceCube DeepCore*, *Eur. Phys. J. C* **82** (2022) 807 [2203.02303].
- [9] ICECUBE collaboration, *Graph neural networks for low-energy event classification and reconstruction in IceCube*, *JINST* **17** (2022) P11003 [2209.03042].
- [10] KM3NeT Collaboration, *The KM3NeT multi-PMT optical module*, *JINST* **17** (2022) P07038 [2203.10048].
- [11] Z.P. Ye et al., *A multi-cubic-kilometre neutrino telescope in the western Pacific Ocean*, *Nature Astron.* **7** (2023) 1497 [2207.04519].
- [12] P-ONE collaboration, *The Pacific Ocean Neutrino Experiment*, *Nature Astron.* **4** (2020) 913 [2005.09493].
- [13] T.-Q. Huang, Z. Cao, M. Chen, J. Liu, Z. Wang, X. You et al., *Proposal for the High Energy Neutrino Telescope*, *PoS ICRC2023* (2023) 1080.
- [14] IceCube-Gen2 Collaboration, M.G. Aartsen et al., *IceCube-Gen2: the window to the extreme Universe*, *J. Phys. G* **48** (2021) 060501 [2008.04323].
- [15] S. Samani et al., *Pulse shape particle identification by a single large hemispherical photomultiplier tube*, *JINST* **15** (2020) T05002 [1912.03901].
- [16] S. Agostinelli et al., *Geant4—a simulation toolkit*, *Nucl. Instrum. Meth. A* **506** (2003) 250.
- [17] ICECUBE collaboration, “OMSim: Geant4 framework for simulating optical modules of the IceCube observatory.” GitHub repository, 2025.
- [18] ICECUBE collaboration, *Measurement of South Pole ice transparency with the IceCube LED calibration system*, *Nucl. Instrum. Meth. A* **711** (2013) 73 [1301.5361].
- [19] C. Andreopoulos et al., *The GENIE Neutrino Monte Carlo Generator*, *Nucl. Instrum. Meth. A* **614** (2010) 87 [0905.2517].
- [20] T. Kozynets, *Atmospheric neutrino oscillations in IceCube-DeepCore within and beyond the unitary framework*, Ph.D. thesis, University of Copenhagen, Faculty of Science, Copenhagen, Denmark, Nov., 2024.
- [21] ICECUBE collaboration, *Refining the IceCube detector geometry using muon and LED calibration data*, *PoS ICRC2023* (2023) 988.
- [22] ICECUBE collaboration, *Calibration and characterization of the IceCube photomultiplier tube*, *Nucl. Instrum. Meth. A* **618** (2010) 139 [1002.2442].
- [23] IceCube Collaboration, *Design and performance of the multi-PMT optical module for IceCube Upgrade*, *PoS ICRC2021* (2021) 1070 [2107.11383].
- [24] KM3NeT Collaboration, *Determining the neutrino mass ordering and oscillation parameters with KM3NeT/ORCA*, *Eur. Phys. J. C* **82** (2022) 26 [2103.09885].

A Supplemental Material

Additional Geant4 figures. Supplementary event displays at 5 and 100 GeV illustrate that the qualitative differences between muon- and electron-induced event morphologies persist across the simulated energy range.

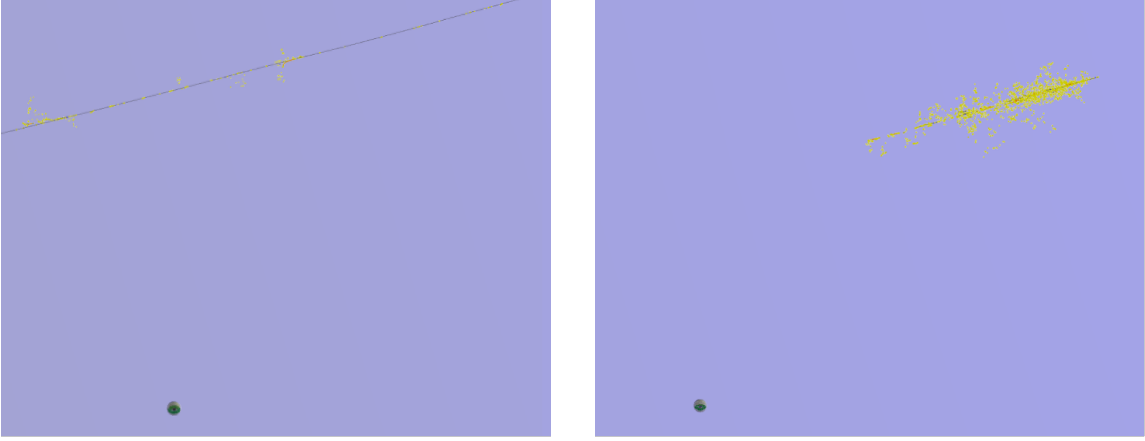


Figure 8: Geant4 OMSim event display of a 5 GeV muon (left) and electron (right) near a DOM. Yellow points indicate the sampled trajectory steps of the charged particles (injected lepton and secondaries), Cherenkov photons are not shown.

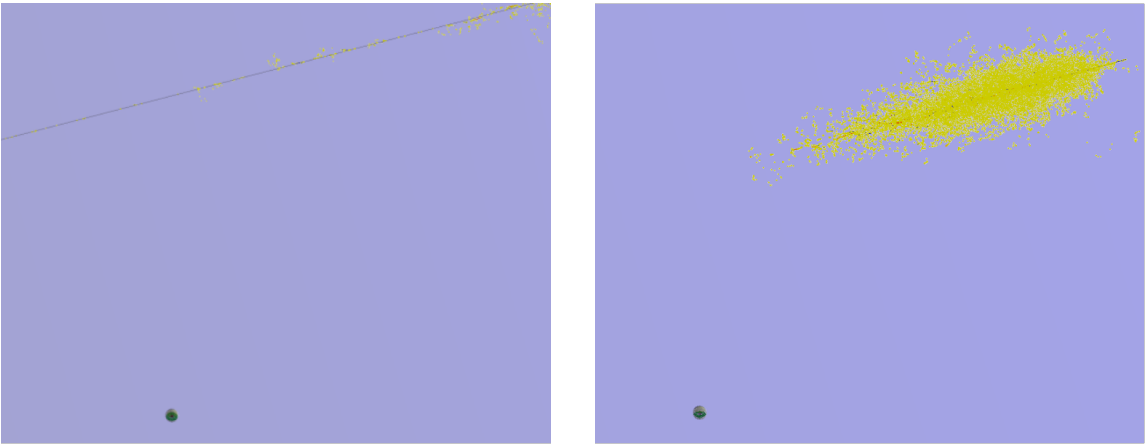


Figure 9: Geant4 OMSim event display of a 100 GeV muon (left) and electron (right) near a DOM. Yellow points indicate the sampled trajectory steps of the charged particles (injected lepton and secondaries), Cherenkov photons are not shown.

When comparing shapes, we use the normalized distribution

$$p(\Delta t_\gamma) \equiv \frac{1}{N_\gamma} \frac{dN_\gamma}{d\Delta t_\gamma}, \quad (\text{A.1})$$

where N_γ is the total number of detected photons for a given energy and distance configuration and Δt_γ is the residual time. This normalization is used to compare the shape of the photon arrival

time distributions in fig. 3 independently of the total photon yield, which differs between muon and electron events. Fig. 10 shows the normalized probability density for the first 16 ns at a fixed impact parameter of 20 m. The muon distribution is more sharply peaked at early times, while the electron distribution is broader, reflecting the extended shower development.

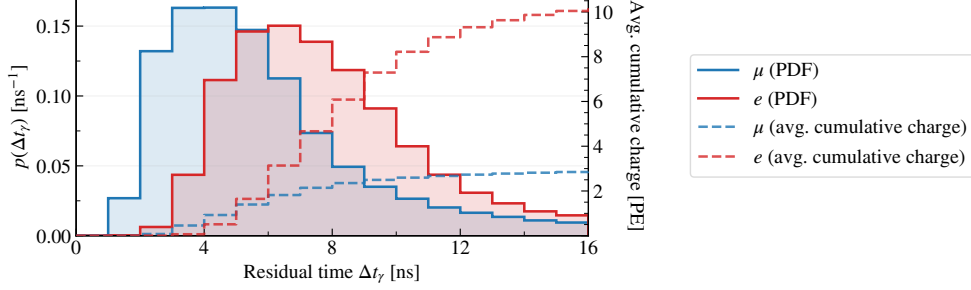


Figure 10: Photon density $p(\Delta t_\gamma)$ for muons and electrons at an impact parameter of 20 m and 50 GeV energy from Geant4 simulations. Dashed curves, read on the right axis, show the corresponding average cumulative detected charge. Both histograms are evaluated in identical 1 ns bins.

Template structure. Fig. 11 shows the resulting template ratio across the full $(\xi^{14\text{ns}}, r, \Delta t)$ feature space, illustrating which regions of the per-DOM observable space drive the track–cascade separation.

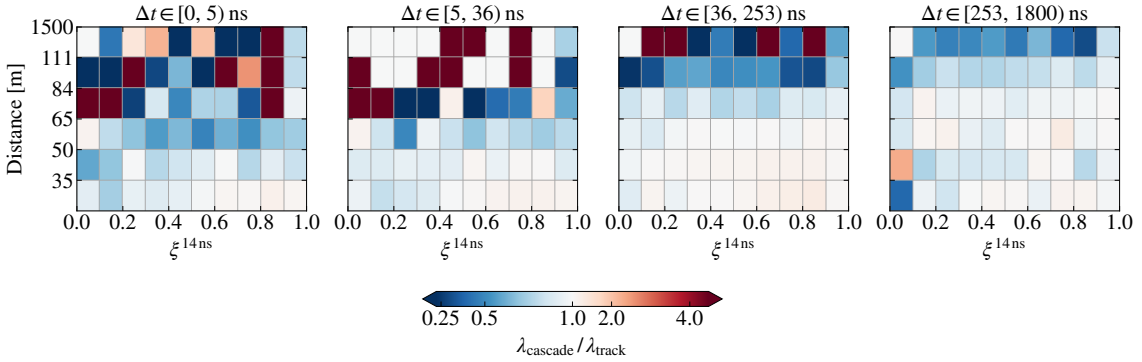


Figure 11: Template ratio $\lambda_{\text{cascade}}/\lambda_{\text{track}}$ in each $(\xi^{14\text{ns}}, r, \Delta t)$ bin. Blue (red) indicates track-like (cascade-like) regions; white corresponds to a ratio of unity or to bins regularized by the floor ε_λ . Discrimination is concentrated in the early-time bin ($\Delta t < 5$ ns) at high $\xi^{14\text{ns}}$ and intermediate distances.

Purity increase. Fig. 12 shows the cascade purity P^C and purity gain ΔP^C on the nominal MC set as functions of selection efficiency ϵ , within the DynEdge cascade PID bin for events with $n_{\text{hit}} \in [10, 20)$. The purity gain is largest at low efficiency and decreases as the threshold is relaxed, reflecting the concentration of discriminating power at high WavePID TS values.

Computational requirements. WavePID is computationally inexpensive. Template construction is performed once from MC and requires storing a three-dimensional histogram with $6 \times 10 \times 4 = 240$

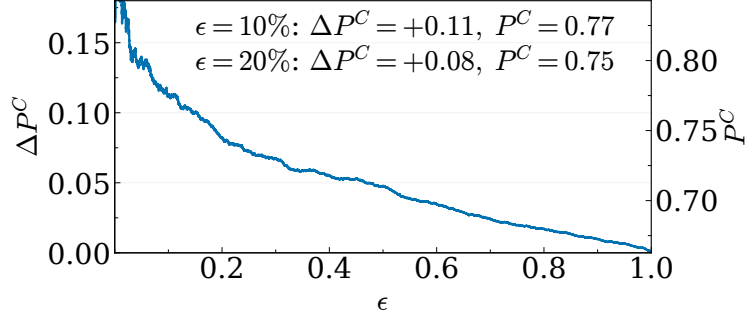


Figure 12: Cascade purity P^C and purity gain ΔP^C as functions of selection efficiency ϵ within the DynEdge cascade PID bin, for events with $n_{\text{hit}} \in [10, 20)$.

bins per class, corresponding to the 6 distance bins, 10 early-charge-fraction bins, and 4 inter-module time bins of eq. (4.1). At inference time, computing the test statistic for a single event involves mapping each DOM’s features to a bin index and summing the corresponding log-odds. This is an $O(n_{\text{hit}})$ operation requiring no matrix multiplications or GPU acceleration. On a single CPU core, WavePID processes $O(10^5)$ events per second, making it suitable for both offline analysis and potential online filtering applications. The memory footprint of the stored templates is less than 10 kB.

Hyperparameter sensitivity. The time window t and bin edges \mathbf{e}_i are set empirically, and the optimal configuration depends on the target metric. Maximizing overall AUC does not necessarily maximize purity at a specific efficiency, and vice versa. The configuration presented here was optimized for AUC in the DynEdge cascade bin with 10–20 hits, yielding a purity increase from 66% to 75% at 20% selection efficiency. Alternative configurations that prioritize purity over broad classification performance can yield higher purity at fixed efficiency, at the cost of reduced AUC.